The Astrophysical Journal, 931:100 (10pp), 2022 June 1 https://doi.org/10.3847/1538-4357/ac6874

Near K-edge Photoionization and Photoabsorption of Singly, Doubly, and Triply Charged Silicon Ions

Stefan Schippers[1], Sebastian Stock[2,3], Ticia Buhr[1], Alexander Perry-Sassmannshausen[1], Simon Reinwardt[4], Michael Martins[4], Alfred Müller[1], and Stephan Fritzsche[2,3,5]
[1] I. Physikalisches Institut, Justus-Liebig-Universität Gießen, Heinrich-Buff-Ring 16, 35392 Giessen, Germany; schippers@jlug.de
[2] Helmholtz-Institut Jena, Fröbelstieg 3, D-07743 Jena, Germany
[3] Theoretisch-Physikalisches Institut, Friedrich-Schiller-Universität Jena, D-07743 Jena, Germany
[4] Institut für Experimentalphysik, Universität Hamburg, Luruper Chaussee 149, D-22761 Hamburg, Germany
[5] GSI Helmholtzzentrum für Schwerionenforschung, Planckstraße 1, 64291 Darmstadt, Germany
Received 2022 March 7; revised 2022 April 11; accepted 2022 April 18; published 2022 May 27

Abstract

Experimental and theoretical results are presented for double, triple, and quadruple photoionization of Si^+ and Si^{2+} ions and for double photoionization of Si^{3+} ions by a single photon. The experiments employed the photon–ion merged-beams technique at a synchrotron light source. The experimental photon-energy range 1835–1900 eV comprises resonances associated with the excitation of a 1*s* electron to higher subshells and subsequent autoionization. Energies, widths, and strengths of these resonances are extracted from high-resolution photoionization measurements, and the core-hole lifetime of K-shell ionized neutral silicon is inferred. In addition, theoretical cross sections for photoabsorption and multiple photoionization were obtained from large-scale multiconfiguration Dirac–Hartree–Fock calculations. The present calculations agree with the experiment much better than previously published theoretical results. The importance of an accurate energy calibration of laboratory data is pointed out. The present benchmark results are particularly useful for discriminating between silicon absorption in the gaseous and in the solid component (dust grains) of the interstellar medium.

Unified Astronomy Thesaurus concepts: Laboratory astrophysics (2004)

1. Introduction

Silicon is a relatively abundant element in the universe and, in particular, a major component of interstellar dust. The binding energy of Si K-shell electrons amounts to about 1840 eV (Deslattes et al. 2003). Correspondingly, Si K-shell absorption by the interstellar medium (ISM) can be observed by X-ray satellites when directed toward distant X-ray emitting cosmic objects such as X-ray binaries (Rogantini et al. 2020). For the correct determination of the silicon abundance in the ISM it is important to know how much silicon is in the gaseous state and how much is (chemically) bound to dust grains (see, e.g., Jenkins 2009). Since high-resolution X-ray absorption spectroscopy is sensitive to chemical shifts of characteristic absorption lines, astrophysical models of the ISM have recently been augmented by absorption coefficients of silicon-containing minerals that were obtained from laboratory measurements at a synchrotron light source (Zeegers et al. 2017, 2019). Here we provide complementary laboratory data for K-shell X-ray absorption by atomic Si^+, Si^{2+}, and Si^{3+} ions that address the gaseous component of the ISM.

Previous experimental work on the photoabsorption of silicon ions considered only absorption by outer electronic shells (Mosnier et al. 2003; Bizau et al. 2009; Kennedy et al. 2014). With the very recent exception of negatively charged Si^- (Perry-Sassmannshausen et al. 2021), K-shell X-ray absorption data for silicon ions were hitherto exclusively obtained from theoretical calculations (Verner et al. 1993; Palmeri et al. 2008; Witthoeft et al. 2011; Kučas et al. 2012, 2015; Hasoglu et al. 2021). Because of the many-body nature of the theoretical problem, the theoretical calculations have to resort to approximations yielding results that bear (usually unknown) uncertainties. In this situation, benchmarking by laboratory experiments (Schippers & Müller 2020) is vital for arriving at sufficiently accurate results that allow one, in the present context, to reliably discriminate between the gaseous and solid components of the ISM.

Similar to our previous work on L-shell ionization of Fe^+, Fe^{2+}, Fe^{3+}, and Ar^+ ions (Schippers et al. 2017; Beerwerth et al. 2019; Müller et al. 2021; Schippers et al. 2021), we have investigated ionization of silicon ions in different charge states. Here, we present experimental and theoretical data for *m*-fold photoionization of Si^{q+} ions with primary charge state *q* leading to the production of Si^{r+} ions with product charge state $r = q + m$

$$h\nu + \mathrm{Si}^{q+} \rightarrow \mathrm{Si}^{r+} + m\mathrm{e}^-. \quad (1)$$

The paper is organized as follows. Section 2 discusses experimental issues, in particular the role of metastable ions in the silicon ion beams and the energy calibration of the photon-energy scale. Section 3 describes calculations of the absorption cross sections and of the complex deexcitation cascades that set in after the initial creation of a K-shell hole. The results are presented and discussed in Section 4 emphasizing their relevance for the identification of gaseous silicon in the ISM. The concluding Section 5 briefly summarizes the findings and provides an outlook on future directions of laboratory astrophysics in the area of atomic inner-shell absorption.

2. Experiment

The measurements were carried out at the synchrotron light source PETRA III operated by DESY in Hamburg, Germany. More specifically, the photon–ion merged-beams technique

(recently reviewed by Schippers et al. 2016b) was employed using the Photon-Ion spectrometer at PETRA III (PIPE) end-station (Schippers et al. 2014; Müller et al. 2017; Schippers et al. 2020) at the photon-beamline P04 (Viefhaus et al. 2013). The beamline's monochromator is equipped with two diffraction gratings with different rulings of 400 and 1200 lines mm^{-1}. The latter was used for the present experiment because it offers the highest photon flux in the photon-energy region of interest. The experimental procedures have been described previously (Schippers et al. 2014; Müller et al. 2017). Therefore, we only provide the details here that are relevant for the presently studied ion species.

Beams of Si^{q+} ions ($q = 1$–3) were produced by evaporating SiO powder from an electrically heated oven into an electron-cyclotron-resonance (ECR) ion source. The ion source was operated on a positive potential of 6 kV such that positively charged ions were accelerated from the ion source toward the electrically grounded ion beamline. Down beam, a dipole electromagnet served for selecting the desired ion species according to their mass-to-charge ratio. Subsequently, the ion beam was collimated and centered onto the counter-propagating photon beam by tuning electrostatic deflectors and lenses appropriately. Typical ion currents in the interaction region were 4.5 nA of $^{28}Si^{+}$ and 2.5 nA of $^{28}Si^{3+}$. The $^{28}Si^{2+}$ ion current was significantly higher (20 nA) since it was heavily contaminated with, e.g., N^{+} or CO^{2+} ions, which have the same mass-to-charge ratio as $^{28}Si^{2+}$. Similarly, it cannot be excluded that the Si^{+} beam was contaminated by N_2^{+} or CO^{+} ions. It has to be pointed out that the product ions with charge states increased by 1, 2, 3, …units can all be individually separated by the dipole magnet (the demerger) in front of the ion detector so that each final channel could be individually investigated.

Relative cross sections for multiple photoionization (see Equation (1)) were determined over a preselected range of photon energies by normalizing the photon-energy-dependent product-ion count rate on the photon flux and on the ion current, which were measured with a calibrated photodiode and a Faraday cup, respectively. For the Si^{3+} primary ions, the relative cross sections were put on an absolute scale by additionally accounting for the separately measured geometrical beam overlap (for details see Schippers et al. 2014; Müller et al. 2017). The uncertainty of the experimental absolute cross-section scale amounts to ±15% (Schippers et al. 2014).

The measurement of absolute cross sections requires a careful adjustment of the mutual overlap of the photon and ion beams. This procedure was only applied to the Si^{3+} ion beam. An experimental determination of absolute cross sections for the multiple ionization of Si^{+} and Si^{2+} primary ions was not possible because of the unknown fractions of contaminating ions in these ion beams. Therefore, the Si^{+} and Si^{2+} cross sections were normalized to theoretical absorption cross sections as explained below.

2.1. Metastable Primary Ions

The Si^{q+} ion beams contained ground-level ions and possibly also unknown fractions of long-lived metastable ions with lifetimes longer than the ions' flight time (a few microseconds) through the apparatus. For aluminum-like Si^{+}, where we assume a statistical population of the experimentally unresolved two fine-structure components of the $3s^2\,3p\,^2P$ ground term, the long-lived metastable levels are the $3s\,3p^2\,^4P_J$ levels with excitation energies of ∼5.3 eV and lifetimes in the range 0.13–1.2 ms (Froese Fischer et al. 2006). Magnesium-like Si^{2+} has long-lived $3s\,3p\,^3P_J$ excited levels with excitation energies of ∼6.6 eV and lifetimes of 58 μs ($J = 1$), 7.8 s ($J = 2$), and ∞ ($J = 0$) with regard to single-photon emission (Froese Fischer et al. 2006). Sodium-like Si^{3+} does not have long-lived singly excited metastable levels. However, the core-excited $2p^5\,3s\,3p\,^4D_{7/2}$ level is metastable against autoionization with a lifetime in the 1–10 μs range (Howald et al. 1986). Its excitation energy is 106 eV (Schmidt et al. 2007).

The fractional populations of metastable excited levels depend on their excitation energies and on the plasma conditions in the ion source. In outer-shell photoionization experiments, their presence is often revealed by characteristic threshold and resonance features in the measured photoionization cross sections. By comparing experimental and theoretical photoionization cross sections Kennedy et al. (2014) inferred a $3s\,3p^2\,^4P$ fraction of about 10% for a Si^{+} ion beam that was also produced with an ECR ion source. Similarly, Mosnier et al. (2003) arrived at a 2%–3% $3s\,3p\,^3P$ fraction of their Si^{2+} ion beam. In the present inner-shell photoionization measurements we did not recognize any specific cross-section features that can be attributed to the presence of metastable levels. Nevertheless, such metastable levels cannot be excluded for the present Si^{+} and Si^{2+} beams similar to in the previous experiments by Kennedy et al. (2014) and Mosnier et al. (2003).

In view of its high excitation energy, one does not expect a significant population of the autoionizing $Si^{3+}(2p^5\,3s\,3p\,^4D_{7/2})$ metastable level. However, even a tiny contamination of the Si^{3+} beam can lead to a noticeable production of Si^{4+} ions via autoionization. In the present experiment, this created a large background in the Si^{3+} single-ionization channel, such that no meaningful experimental result could be obtained for the production of Si^{4+} by photoionization of Si^{3+}. We conclude that, apart from this limitation, metastable primary ions do not play a significant role in the present study.

2.2. Photon-energy Calibration

The photon-energy scale was calibrated by a separate measurement of the krypton L_3 and L_2 absorption edges at about 1677 and 1730 eV (Figure 1) using a combination of a gas jet and a photoelectron spectrometer (see Müller et al. 2017, 2018, for details). The recommended values for the Kr L_3 and L_2 threshold energies are 1679.07(39) and 1730.90(50) eV (Deslattes et al. 2003). Unfortunately, it is not clear where to read these values off the measured absorption curves. Therefore, we have applied energy shifts to our measured data such that the presently measured krypton absorption edges line up with the corresponding absorption curves of Wuilleumier (1971) as displayed in Figure 1.

Wuilleumier (1971) provided wavelengths in Cu x units referring to the Cu $K\alpha_1$ line. For the conversion of these units to electronvolts, the CODATA 2018 set of fundamental physical constants was used (Tiesinga et al. 2021). The resulting conversion factor agrees with the one provided earlier by Deslattes et al. (2003) within its negligible (in the present context) uncertainty.

Absorption at the Kr L_3 and L_2 edges was also measured by others. The results of Kato et al. (2007) differ from those of Wuilleumier (1971) by ∼1.25 and ∼0.55 eV, respectively.

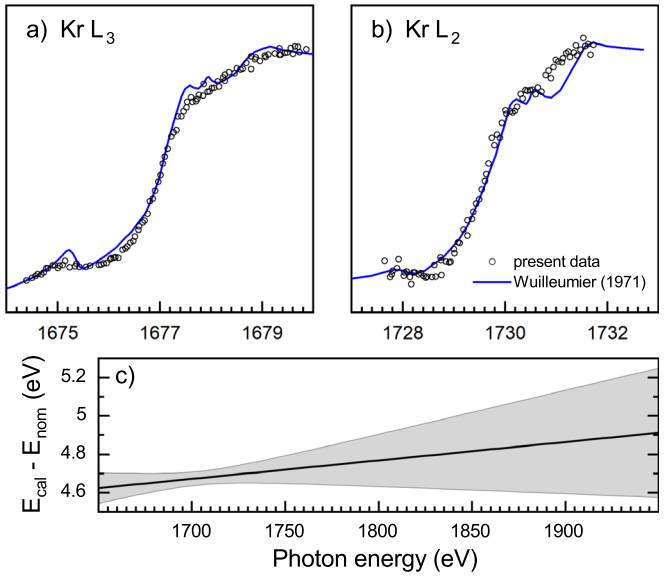

Figure 1. Calibration of the photon-energy scale by shifting the present krypton absorption data (symbols) to the experimental results of Wuilleumier (1971; solid lines, digitized) for the L_3 and L_2 absorption edges displayed in panels (a) and (b), respectively. The solid line in panel (c) is the extrapolated difference between calibrated photon energies $E_{\rm cal}$ and nominal photon energies $E_{\rm nom}$ for the entire energy range of interest. The gray shaded area visualizes the associated uncertainties as determined from error propagation (see the text). In all panels, the abscissae are the calibrated photon energy.

Kato et al. (2007) calibrated their energy scale to the Kr $2p_{3/2}^{-1}5p$ excitation energy in the vicinity of the L_3 threshold as determined by Ibuki et al. (2002). These latter authors did not provide an estimate for the uncertainty of their energy scale. The same holds for the Kr L_3 absorption measurements of Schmelz et al. (1995). Nagaoka et al. (2000) and Okada et al. (2005) calibrated their energy scales by referring to the work of Wuilleumier (1971) as is also done here.

The energy shifts applied to our absorption curves were 4.65 and 4.7 eV for the L_3 edge and the L_2 edge, respectively. We attribute a read-off uncertainty of 0.05 eV to this calibration method. For the extrapolation to higher energies we used a linear fit through the two calibration points. By this extrapolation, the read-off error propagates to energy uncertainties of $\pm$0.2 eV at 1840 eV and of $\pm$0.3 eV at 1920 eV (Figure 1(c)). Taking the 0.5 eV uncertainty of the recommended L_2-threshold energy (Deslattes et al. 2003) and a 0.2 eV uncertainty associated with imperfections of the photon beamline (see Section 4.3) additionally into account, we arrive at an uncertainty of $\pm$ 1 eV of the present calibrated photon-energy scale for the photon energies in the current experimental range of 1835–1900 eV.

In calibrating the photon-energy scale of the silicon ions, we have additionally considered the Doppler shift that is caused by the unidirectional movement of the ions in the Si^{q+} ion beams (see, e.g., Schippers et al. 2014, for details). This does not introduce any significant additional uncertainty of the photon-energy calibration.

3. Theory

The present theoretical calculations were performed in the framework of the multiconfiguration Dirac–Hartree–Fock (MCDHF) method by applying the GRASP (Jönsson et al. 2007) and RATIP (Fritzsche 2012) atomic structure codes for the calculation of atomic energy levels and transition rates. In particular, the Auger cascades were analyzed and calculated following the creation of a K-shell hole in initially Si^{q+} ions by direct $1s$ ionization or by $1s \rightarrow np$ excitation. These cascade computations (Fritzsche et al. 2021) support quantitative estimates for the distribution of Si^{r+} product ions (see Equation (1)), similar to earlier studies for other atoms and ions (Beerwerth & Fritzsche 2017; Stock et al. 2017; Schippers et al. 2017, 2021; Buth et al. 2018; Beerwerth et al. 2019).

In these cascade computations, the Si^{q+} ions were assumed to be initially in their respective ground configuration with statistically populated fine-structure levels. Cross sections for the direct photoionization of these ions were obtained for each atomic subshell, while the resonant $1s \rightarrow np$ photoexcitation was considered for all shells with $3 \leqslant n \leqslant 7$ for Si^+ and $3 \leqslant n \leqslant 8$ for Si^{2+} and Si^{3+}. From the incoherent summation of all these direct-photoionization and resonant-excitation contributions, the total photoabsorption cross sections were determined for Si^+, Si^{2+}, and Si^{3+} ions.

While different autoionization processes might contribute to the electron emission from inner-shell excited ions, only those single-step Auger processes that are energetically allowed in a configuration-averaged representation of the atomic fine structure were taken into account into the casecase. This simplifies the cascade computations and makes them tractable, although further contributions from the simultaneous excitation (shake-up) or ionization (shake-off) of another electron were found essential for accurately predicting the final charge-state distributions of light and especially negatively charged ions (Müller et al. 2015; Schippers et al. 2016a; Perry-Sassmannshausen et al. 2020). For multiply charged ions, however, these shake processes are typically suppressed, though not always negligible. Table 1 lists all of the electron configurations that were included in the present cascade computations for Si^+ ions. The number of cascade steps, i.e., the so-called depth of the cascade, were taken to be four for Si^+, three for Si^{2+} , and two for Si^{3+}. For the analysis of the cascades, therefore, the highest product-ion charge state was $r = 5$ (see Equation (1)), while higher charge states were not accessible within the given approach and by excluding autoionization processes with an additional excitation or ionization of electrons.

Theoretical cross sections for multiple photoionization were eventually obtained by multiplying the calculated absorption cross sections with the branching ratios from the cascade computations. These computations were carried out separately for the different $1s$ core-ionized and $1s \rightarrow np$ core-excited configurations. For the comparison with the experimental results, the theoretical cross sections were convolved with a Gaussian with the FWHM corresponding to the experimental photon-energy spread ΔE.

4. Results and Discussion

4.1. Cross Sections for Multiple Ionization

Figure 2 provides an overview of the measured and calculated cross sections $\sigma_{q,r}$ for multiple photoionization of Si^{q+} ions (see Equation (1)) with primary charge states $q = 1$, 2, 3 together with the cross-section sums

$$\sigma_{q,\Sigma} = \sum_r \sigma_{q,r}. \tag{2}$$

The experimental energy ranges comprise the thresholds for direct ionization of one K-shell electron. The experimental

Table 1
Configurations That Are Taken into Account in the Present Calculations of the Deexcitation Cascades Following the Direct $1s$ Ionization and the $1s \rightarrow 3p$ Excitation of Si^+

Ion	$1s$ Ionization	$1s \rightarrow 3p$ Excitation
Si^+		$1s^1\,2s^2\,2p^6\,3s^2\,3p^2$
Si^{2+}	$1s^2\,2s^2\,2p^6\,3s^2$	$1s^2\,2s^2\,2p^6\,3s^2$
	$1s^2\,2s^2\,2p^6\,3s^1\,3p^1$	$1s^2\,2s^2\,2p^6\,3s^1\,3p^1$
	$1s^2\,2s^2\,2p^5\,3s^2\,3p^1$	$1s^2\,2s^2\,2p^6\,3p^2$
	$1s^2\,2s^2\,2p^5\,3s^1\,3p^2$	$1s^2\,2s^2\,2p^5\,3s^2\,3p^1$
	$1s^1\,2s^2\,2p^6\,3s^2\,3p^1$	$1s^2\,2s^2\,2p^5\,3s^1\,3p^2$
		$1s^2\,2s^1\,2p^6\,3s^2\,3p^1$
		$1s^2\,2s^1\,2p^6\,3s^1\,3p^2$
		$1s^2\,2s^2\,2p^4\,3s^2\,3p^2$
		$1s^2\,2s^1\,2p^5\,3s^2\,3p^2$
		$1s^2\,2p^6\,3s^2\,3p^2$
Si^{3+}	$1s^2\,2s^2\,2p^6\,3s^1$	$1s^2\,2s^2\,2p^6\,3s^1$
	$1s^2\,2s^2\,2p^6\,3p^1$	$1s^2\,2s^2\,2p^6\,3p^1$
	$1s^2\,2s^2\,2p^5\,3s^2$	$1s^2\,2s^2\,2p^5\,3s^2$
	$1s^2\,2s^2\,2p^5\,3s^1\,3p^1$	$1s^2\,2s^2\,2p^5\,3s^1\,3p^1$
	$1s^2\,2s^1\,2p^6\,3s^2$	$1s^2\,2s^2\,2p^5\,3p^2$
	$1s^2\,2s^1\,2p^6\,3s^1\,3p^1$	$1s^2\,2s^1\,2p^6\,3s^2$
	$1s^2\,2s^2\,2p^4\,3s^2\,3p^1$	$1s^2\,2s^1\,2p^6\,3s^1\,3p^1$
	$1s^2\,2s^1\,2p^5\,3s^2\,3p^1$	$1s^2\,2s^1\,2p^6\,3p^2$
	$1s^2\,2p^6\,3s^2\,3p^1$	$1s^2\,2s^2\,2p^4\,3s^2\,3p^1$
		$1s^2\,2s^2\,2p^4\,3s^1\,3p^2$
		$1s^2\,2s^1\,2p^5\,3s^2\,3p^1$
		$1s^2\,2s^1\,2p^5\,3s^1\,3p^2$
Si^{4+}	$1s^2\,2s^2\,2p^6$	$1s^2\,2s^2\,2p^6$
	$1s^2\,2s^2\,2p^5\,3s^1$	$1s^2\,2s^2\,2p^5\,3s^1$
	$1s^2\,2s^2\,2p^5\,3p^1$	$1s^2\,2s^2\,2p^5\,3p^1$
	$1s^2\,2s^1\,2p^6\,3s^1$	$1s^2\,2s^1\,2p^6\,3s^1$
	$1s^2\,2s^1\,2p^6\,3p^1$	$1s^2\,2s^1\,2p^6\,3p^1$
	$1s^2\,2s^2\,2p^4\,3s^2$	$1s^2\,2s^2\,2p^4\,3s^2$
	$1s^2\,2s^2\,2p^4\,3s^1\,3p$	$1s^2\,2s^2\,2p^4\,3s^1\,3p^1$
	$1s^2\,2s^1\,2p^5\,3s^2$	$1s^2\,2s^2\,2p^4\,3p^2$
	$1s^2\,2s^1\,2p^5\,3s^1\,3p^1$	
Si^{5+}	$1s^2\,2s^2\,2p^5$	$1s^2\,2s^2\,2p^5$
	$1s^2\,2s^1\,2p^6$	
	$1s^2\,2s^2\,2p^4\,3s^1$	

Note. All in all, nearly a quarter million of level-to-level transition rates had to be calculated to describe the cascade processes.

photon-energy spread was $\Delta E \approx 3$ eV. This is sufficient for resolving the individual $1s \rightarrow np$ resonance groups for $n = 3$ and $n = 4$. For Si^{3+}, even the $1s \rightarrow 5p$ resonance group can be discerned.

The logarithmic cross-section scales cover up to 4 orders of magnitude. For Si^+, the main ionization channel is triple ionization. For Si^{2+}, triple ionization dominates only for energies above ~1875 eV where direct K-shell ionization becomes energetically possible. At lower energies, double ionization is stronger. For Si^{3+}, double ionization is the dominating ionization channel in the entire experimental photon-energy range. The single-ionization channel could not be measured as explained above (Section 2.1). Other Si^{3+} ionization channels were scrutinized, but no detectable signal was found. This indicates that the associated cross sections are small, as is also corroborated by our theoretical calculations.

Our theoretical ab initio cross sections are in remarkable agreement with the measured ones considering the simplifications that had to be applied in order to make the calculations of the complex deexcitation cascades tractable. We like to point out that the calculations were performed independently of the measurements.

The experimental and theoretical resonances line up if energy shifts of −1.7, −1.8, and −1.2 eV are applied to the theoretical Si^+, Si^{2+}, and Si^{3+} cross sections, respectively. These differences between our theoretical and experimental resonance positions are less than a factor of 2 larger than the 1 eV uncertainty of the experimental energy scale. Our theoretical calculations do not account for any of the metastable primary ions discussed in Section 2.1. The comparison between the theoretical and the experimental resonance structures suggests that metastable ions do indeed not play a significant role in the present study as already concluded above.

Only the theoretical and experimental cross sections $\sigma_{3,5}$ can be directly compared on an absolute scale. The mutual agreement is within the ± 15% experimental uncertainty over nearly the entire experimental energy range. The largest discrepancy between the experimental and present theoretical cross sections concerns the (small) Si^+ double-ionization cross section, which is underestimated by a factor of ~2. At energies between 1845 and 1858 eV, slight discrepancies occur, which are due to a limited ability of the theory to correctly describe the experimentally observed resonance structure. There are no such obvious discrepancies for Si^+ and Si^{2+}.

We conclude that the present theoretical approach is capable of reliably predicting the multiple photoionization cross sections of low-charged silicon ions. Similar accuracy can be expected for neighboring elements from the periodic table. The benchmarking by our experimental results leads to rather small corrections of the theoretical resonance energies, which are only slightly larger than the uncertainty of the present experimental photon-energy scale.

4.2. Absorption Cross Sections

For Si^+ and Si^{2+}, the experimental cross-section sums $\sigma_{q,\Sigma}$ were put on absolute scales by multiplying all individual cross sections $\sigma_{q,r}$ for a given primary charge state q by the same factor such that the sums line up with the respective theoretical absorption cross sections of Verner et al. (1993, Figures 3(b)–(d)). We have applied the same approach already earlier to the photoabsorption of negatively charged Si^- ions (Perry-Sassmannshausen et al. 2021) where we used the theoretical absorption cross section for neutral silicon by Henke et al. (1993) as a reference. These data are shown in Figure 3(a) for comparison. Apparently, the cross sections for nonresonant absorption are nearly independent of the primary charge state. At 1890 eV the cross sections for Si^0 (Henke et al. 1993) and for Si^+, Si^{2+}, and Si^{3+} (Verner et al. 1993) all amount to about 0.15 Mb.

For energies where there are no signatures from resonant processes, our theoretical cross-section sums for Si^+, Si^{2+}, and Si^{3+} agree with the results of Verner et al. (1993), which do not account for resonant photoabsorption. The same is true for the more recent theoretical results of Witthoeft et al. (2011), who also included resonant photoabsorption in their calculations. However, their resonance positions deviate significantly by up to ~9 eV from the measured ones. Our present energy-shifted (by less than 2 eV, see Section 4.1) theoretical results fit much better to the experimentally observed resonance positions than the results of Witthoeft et al. (2011).

Another significant discrepancy between the present and the previous results concerns the thresholds for direct K-shell

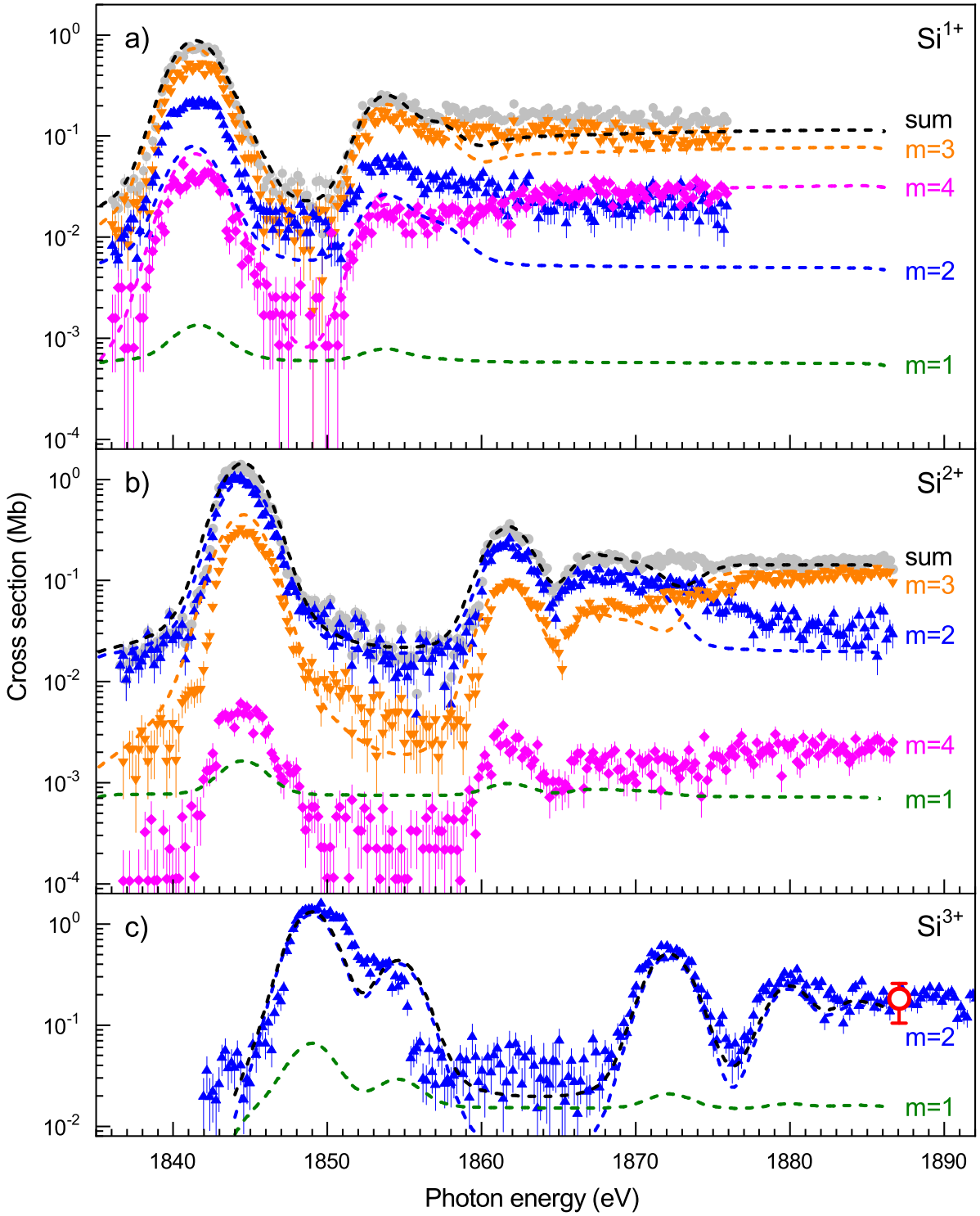

Figure 2. Experimental cross sections for double (blue triangles, $m = 2$), triple (orange inverted triangles, $m = 3$), and quadruple (magenta diamonds, $m = 4$) photoionization of (a) Si^+, (b) Si^{2+}, and (c) Si^{3+}. The gray circles in panels (a) and (b) represent the sum (Equation (2)) of the cross sections $\sigma_{1,\Sigma} = \sigma_{1,3} + \sigma_{1,4} + \sigma_{1,5}$ and $\sigma_{2,\Sigma} = \sigma_{2,4} + \sigma_{2,5} + \sigma_{2,6}$, respectively. For Si^{3+}, only the double-ionization cross section $\sigma_{3,5}$ was measured. The open circle at ~1887 eV in panel (c) represents the measured absolute data point. Its error bar comprises the statistical uncertainty and a 15% systematic uncertainty. The dashed curves are the present theoretical results for single ionization (olive), double ionization (blue), triple ionization (orange), and quadruple ionization (magenta). The black dashed curves are the corresponding cross-section sums. The theoretical cross sections were convolved with a Gaussian with an FWHM of $\Delta E = 3$ eV corresponding to the experimental photon-energy spread and shifted by (a) −1.7 eV, (b) −1.8 eV, and (c) −1.2 eV in order to line up the theoretical resonance features with the experimental ones. Single ionization could not be measured due to the low cross sections and comparatively high background levels, particularly for Si^{3+} where a strong background was caused by autoionizing metastable levels (see Section 2.1).

photoionization. Our theoretical results are 1860, 1874, and 1891 eV for Si^+, Si^{2+}, and Si^{3+}, respectively, with the abovementioned energy shifts applied. As can be seen from Figure 3, the threshold energies as predicted by Verner et al. (1993) are lower by more than 20 eV. This shows that our experimental benchmarks are vital for arriving at an accurate

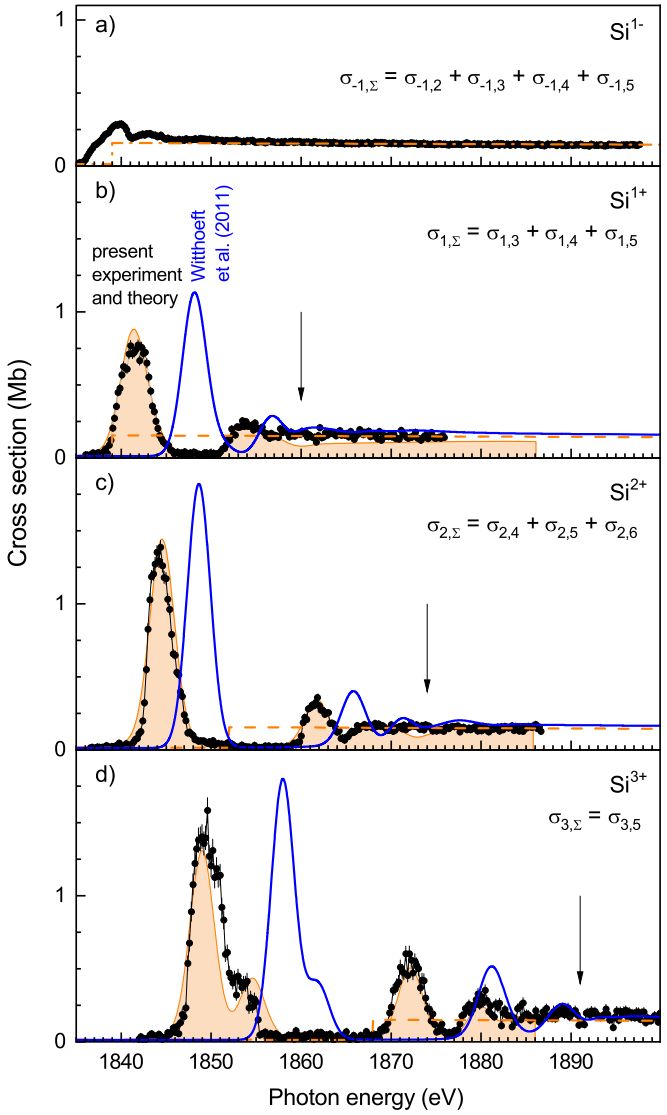

Figure 3. (a) Experimental cross-section sum (symbols) for negatively charged silicon ions (Perry-Sassmannshausen et al. 2021). The dashed–dotted curve is the photoabsorption cross section for neutral silicon atoms as recommended by Henke et al. (1993). (b), (c), and (d) Experimental cross-section sums (symbols) from Figure 2 for Si^+, Si^{2+}, and Si^{3+}, respectively, in comparison with corresponding present theoretical photoabsorption cross sections (shaded curves) and those of Verner et al. (1993, dashed curves) and Witthoeft et al. (2011, solid blue curves). For the comparison, the theoretical cross sections were convolved with a Gaussian with an FWHM of 3 eV in order to account for the experimental photon-energy spread. In addition, the present theoretical cross sections were shifted by −1.7 eV, −1.8 eV, and −1.2 eV, respectively, in order to line up the theoretical resonance features with the experimental ones. The vertical arrows mark the present theoretical thresholds for direct K-shell ionization with the above energy shifts applied.

positioning of the various absorption features. From the comparison with the theoretical absorption cross sections we conclude that, within the present experimental uncertainties, the experimental cross-section sums $\sigma_{q,\Sigma}$ represent the Si^{q+} photoabsorption cross sections.

4.3. High-resolution Measurements of Resonances

The most prominent resonance feature in each absorption cross section is the lowest-energy resonance group, which is associated with $1s \rightarrow 3p$ excitation (Figure 3). Its relative strength increases with increasing primary charge state. This also holds for the resonances associated with $1s$ excitation to higher np subshells. In order to provide accurate resonance data we have measured the most prominent resonance features at lower photon-energy spreads. This was achieved at the expense of photon flux by narrowing the monochromator exit-slit.

Figure 4 displays high-resolution measurements of the $Si^+(1s^{-1}\,3s^2\,3p^2)$ resonance group, which consists of the four LS terms ^2S, ^2P, ^4P, and ^2D resulting from the coupling of the single $1s$ electron to the three $3p^2$ parent terms ^1S, ^3P, and ^1D. For these measurements the dominant triple-ionization channel ($\sigma_{1,4}$) was chosen. The experimental resolving power increases when going from panel (a) to panel (d). The numerical values of the respective photon-energy spreads ΔE were obtained by a simultaneous fit of four Voigt line profiles to the four measured data sets. The resonance parameters that resulted from the fit, i.e., the resonance energies E_r, the Lorentzian line widths Γ, and the resonance strengths $S_{1,4}$ are listed in Table 2.

In the fit, an overall energy shift was used as an additional fit parameter individually for each data set (see the caption of Figure 4). The maximum shift amounts to −0.19 eV, which is much less than the 1 eV uncertainty of the experimental photon-energy scale. Ideally, one would expect that the resonance positions were independent of the width of the monochromator's exit-slit. We attribute the observed shifts to a slight asymmetry of the photon-energy distribution and to mechanical imperfections of the photon-beamline's mechanics. A pertaining 0.2 eV uncertainty has already been considered in the error budget of our photon-energy calibration (see Section 2.2).

In analogy to the work of Schlachter (2004) for carbon, we note that the $1s^{-1}\,3s^2\,3p^2\,^2P$ and $1s^{-1}\,3s^2\,3p^2\,^4P$ levels, which are populated by $1s \rightarrow 3p$ excitation of Si^+, can also be prepared by the removal of a $1s$ electron from neutral ground-term neutral $Si(1s^2\,3s^2\,3p^2\,^3P)$. Therefore, the widths of the $1s^{-1}\,3s^2\,3p^2\,^2P$ and $1s^{-1}\,3s^2\,3p^2\,^4P$ levels from Table 2 correspond to the core-hole lifetime τ of initially neutral silicon. Both widths agree within their experimental uncertainties. From the less uncertain value we obtain $\tau = h/\Gamma = 1.4 \pm 0.5$ fs in agreement with the present calculations and with the value of 1.47 fs calculated by Palmeri et al.(2008).

In Figure 4(d), the present theoretical results for $\sigma_{1,4}$ are compared with the experimental high-resolution results. For the comparison, the theoretical resonances were shifted in energy by −1.7 eV and convoluted with a Gaussian with an FWHM of 0.3 eV. This resolution is a factor of 10 higher as compared to the one in Figure 3 and reveals some discrepancies between experiment and theory, which are missed when looked at with larger photon-energy spread. The calculated splittings between the various $1s^{-1}\,3s^2\,3p^2$ terms are larger than what is found experimentally.

The computed resonance strengths of individual terms contributing to $\sigma_{1,4}$ (see Figure 4(d)) are larger than the experimental ones by about 50%. Since the present theoretical and experimental absorption cross sections $\sigma_{1,\Sigma}$ agree with one another within the experimental uncertainty (Figure 3(b)) it must be concluded that the mismatch for $\sigma_{1,4}$ is due to the overestimation of the corresponding branching ratios for the $1s^{-1}\,3s^2\,3p^2$ resonances.

The theoretical branching ratios for the triple-ionization channel are almost the same for all of the $1s^{-1}\,3s^2\,3p^2$ resonances, i.e., their differences are smaller than the

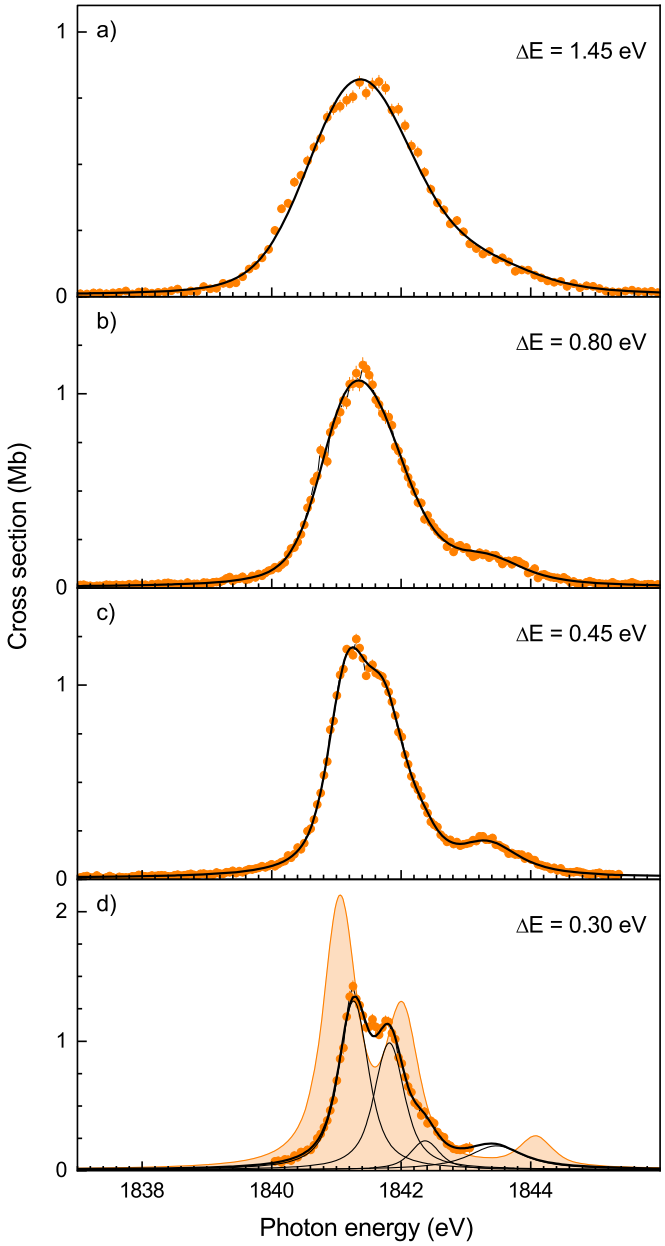

Figure 4. Measured cross sections $\sigma_{1,4}$ for triple photoionization of Si^+ ions using different photon-energy spreads ΔE of (a) 1.45 eV (500 μm), (b) 0.80 eV (250 μm), (c) 0.45 eV (100 μm), and (d) 0.30 eV (20 μm) with the numbers in parentheses denoting the nominal monochromator exit-slit widths. The thick solid lines represent the results from fits of the sum of four Voigt line profiles to the measured data. The four data sets were fitted simultaneously using a common set of resonance parameters. The resulting fit values are listed in Table 2. The individual line profiles are visualized by the thin solid lines in panel (d). Additional fit parameters were ΔE (the Gaussian FWHM, $\pm$0.02 eV fit uncertainty in all cases), a constant background (practically negligible), and an overall energy shift amounting to (a) -0.19 ± 0.01 eV, (b) -0.150 ± 0.007 eV, (c) -0.089 ± 0.005 eV, and (d) 0 eV.The shaded curves in panel (d) are the present theoretical cross section $\sigma_{1,4}$ shifted in energy by -1.7 eV and convolved with a Gaussian with an FWHM of 0.3 eV.

uncertainties of the individual $S_{1,4}$ values. This allows us to scale the fitted individual resonance strengths to the absorption cross section. From a fit to the $1s^{-1}\,3s^2\,3p^2$ peak in Figure 3(b) we obtain a strength of 3.15(17) Mb eV for the sum of the four tabulated resonances. The sum of the $S_{1,4}$ values in Table 2 amounts to 2.02(17) Mb eV. Using these values we have calculated the tabulated absorption resonance-strengths as

Table 2
Results of the Resonance Fits to the Si^+ High-resolution Data ($\sigma_{1,4}$) for the $1s^{-1}\,3s^2\,3p^2$ Resonance Group (Figure 4)

Designation	E_r (eV)	Γ (eV)	$S_{1,4}$ (Mb eV)	S_Σ (Mb eV)
$1s^{-1}\,3s^2\,3p^2\,{}^2P$	1841.26(1)	0.38(22)	0.91(07)	1.42(11)
$1s^{-1}\,3s^2\,3p^2\,{}^2D$	1841.82(1)	0.39(09)	0.70(14)	1.09(22)
$1s^{-1}\,3s^2\,3p^2\,{}^4P$	1842.35(5)	0.34(13)	0.15(07)	0.23(11)
$1s^{-1}\,3s^2\,3p^2\,{}^2S$	1843.43(2)	0.94(04)	0.26(01)	0.41(02)

Note. The resonance energies E_r, Lorentzian line widths Γ, and resonance strength $S_{1,4}$ were obtained from fitting Voigt line profiles to the experimental data. The column labeled by S_Σ contains the derived absorption line strengths (see the text). Numbers in parentheses denote the uncertainties that were obtained from the fit 1 Mb $= 10^{-18}$ cm^2.

Table 3
Results of the Resonance Fits to the Si^{2+} High-resolution Data ($\sigma_{2,4}$) for the $1s^{-1}\,3s^2\,np$ Resonance Groups with $n = 3, 4, 5$ (Figure 5)

Designation	E_r (eV)	Γ (eV)	$S_{2,4}$ (Mb eV)	S_Σ (Mb eV)
$1s^{-1}\,3s^2\,3p\,{}^1P$	1845.10(01)	0.28(03)	2.48(16)	3.33(22)
$1s^{-1}\,3s^2\,3p\,{}^3P$	1845.84(15)	0.76(14)	0.72(16)	0.97(22)
$1s^{-1}\,3s^2\,4p\,{}^1P$	1862.33(24)	0.37(08)	0.55(10)	0.60(11)
$1s^{-1}\,3s^2\,4p\,{}^3P$	1863.10(20)	1.77(37)	0.48(18)	0.52(20)
$1s^{-1}\,3s^2\,5p\,{}^1P$	1867.58(08)	0.00(20)	0.07(05)	
$1s^{-1}\,3s^2\,5p\,{}^3P$	1867.85(08)	0.84(15)	0.32(08)	

Note. For the explanation of the notation see Table 2.

Table 4
Results of the Resonance Fits to the Si^{3+} High-resolution Data ($\sigma_{3,5}$) for the $1s^{-1}\,3s\,np$ Resonance Groups with $n = 3, 4, 5$ (Figure 6)

Designation	E_r (eV)	Γ (eV)	$S_{3,5}$ (Mb eV)	S_Σ (Mb eV)
$1s^{-1}\,3s\,3p(^3P)^2P$	1849.64(01)	0.45(02)	5.20(09)	5.20(09)
$1s^{-1}\,3s\,3p(^1P)^2P$	1853.24(01)	0.35(04)	1.23(06)	1.23(06)
$1s^{-1}\,3s\,4p(^3P)^2P$	1871.91(02)	0.34(05)	1.19(08)	1.19(08)
$1s^{-1}\,3s\,4p(^1P)^2P$	1872.96(04)	0.45(12)	0.56(08)	0.56(08)
$1s^{-1}\,3s\,5p\,{}^2P$	1880.20(05)	1.00(44)	0.79(06)	0.79(06)
$1s^{-1}\,3s\,6p\,{}^2P$	1883.86(04)	0.23(12)	0.25(04)	0.25(04)

Note. For the explanation of the notation see Table 2.

$S_\Sigma = S_{1,4} \times 3.15/2.02$. In the same way we have calculated S_Σ separately for the $1s^{-1}\,3s^2\,3p$ [factor 4.30(3)/3.20(22)] and $1s^{-1}\,3s^2\,4p$ [factor (1.12(4)/1.03(21)] resonances of the Si^{2+} absorption spectrum (Table 3). For Si^{3+}, the absorption spectrum is essentially identical with $\sigma_{3,5}$ and, thus, $S_\Sigma = \sigma S_{3,5}$ for all resonances in Table 4.

The fits to the Si^{2+} and Si^{3+} high-resolution data are shown in Figures 5 and 6, respectively. The agreement between experiment and the present theory (shifted by -1.8 eV for Si^{2+} and by -1.2 eV for Si^{3+}, see Figure 3) is remarkable, particularly for $\sigma_{2,4}$ (Figure 5). There is less agreement for Si^{3+}, as already noted in the low-resolution data in Figures 2 and 3. The too large separation of the first two peaks is probably caused by subtleties concerning the atomic fine structure associated with the angular momentum coupling of three open atomic subshells.

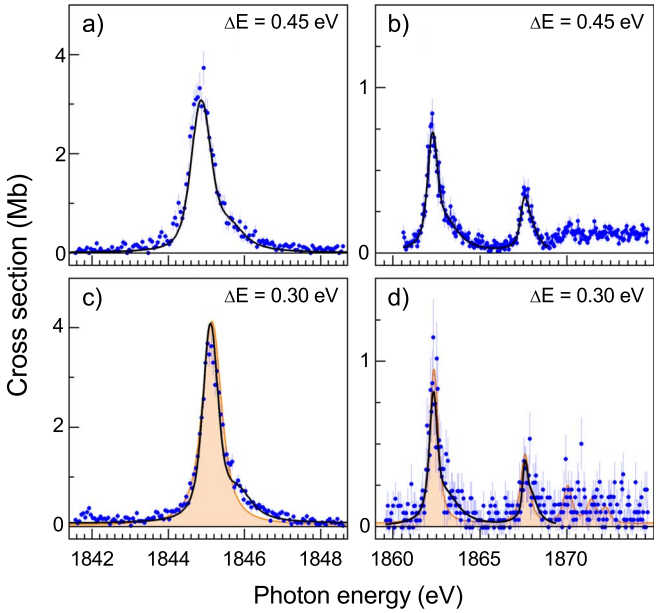

Figure 5. Measured cross sections $\sigma_{2,4}$ for double photoionization of Si^{2+} ions using different photon-energy spreads $\Delta E = 0.45$ eV and $\Delta E = 0.30$ eV. The thick solid lines represent the results from fits of the sum of two (for (a) and (c)) and four (for (b) and (d)) Voigt line profiles to the measured data. The data sets in panels (a) and (c) were fitted simultaneously using a common set of resonance parameters. The same holds for the data sets from panels (b) and (d). The resulting fit values are listed in Table 3. In panel (c), the individual line profiles are visualized by the thin solid lines. Additional fit parameters were ΔE (kept fixed), a constant background (subtracted) and an overall energy shift amounting to (a) -0.26 ± 0.02 eV, (b) -0.05 ± 0.02 eV, (c) 0 eV, and (d) 0 eV. The shaded curve in panels (c) and (d) is the present theoretical cross section $\sigma_{2,4}$ shifted in energy by -1.8 eV and convolved with a Gaussian with an FWHM of 0.3 eV.

4.4. Comparison with Other Forms of Silicon

Figure 7 shows a comparison between the strongest Si K-shell absorption features for Si^+, Si^{2+}, and Si^{3+} (panel (a)) with the absorption by some silicon-containing minerals that potentially occur in interstellar dust (panel (b); Zeegers et al. 2019). In order to be able to discriminate between the different forms of silicon in X-ray absorption spectra, the energies of the absorption features must be known with sufficient precision. The systematic uncertainty of the present experimental energy scale is ± 1 eV (Section 2.2). Zeegers et al. (2019) did not quantify the uncertainty of their energy scale. Instead, for their energy calibration they referred to previous works (Li et al. 1995; Nakanishi & Ohta 2009), which, in turn, are based on earlier investigations. The energy scale of Nakanishi & Ohta (2009) can be traced back to the work of Wong et al. (1999) who mention that their energy calibration varies by 2–3 eV depending on the operating conditions of their synchrotron light source. This suggests that the uncertainty of the energy scale of (Zeegers et al. 2019; Figure 7(b)) is at least ± 1.5 eV.

Different minerals exhibit different chemical shifts of the Si K-shell absorption features, which vary by up to 1.5 eV (Li et al. 1995). This is still less than the combined energy uncertainties of the present energy scale and the one of Zeegers et al. (2019). Therefore, we conclude that, in general, X-ray absorption spectroscopy can discriminate between absorption by gaseous silicon and absorption by silicon-containing minerals. In particular, the Si^+ absorption featured in Figure 7(a) appears at an unambiguous location ($\sim$1841.5 eV). This is also true for the corresponding absorption feature of Si^-, which occurs at an even lower energy of 1838.4 eV (Figure 3(a); Perry-Sassmannshausen et al. 2021). To the best of our knowledge, there are no such experimental data for gaseous neutral silicon. In view of the findings for Si^- and Si^+ its dominating absorption feature can be expected close to 1840 eV.

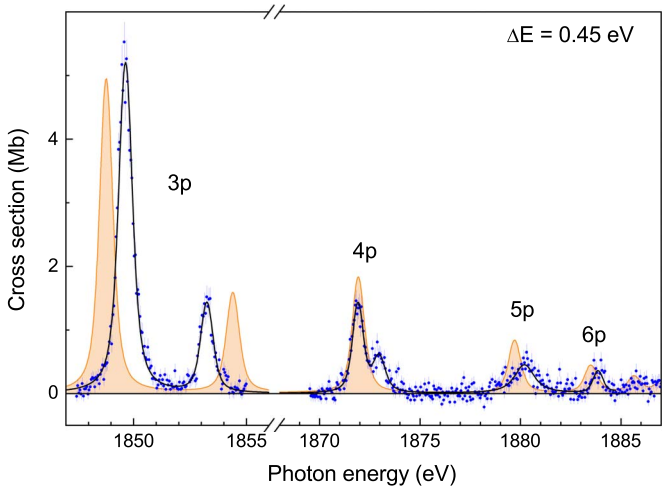

Figure 6. Measured (symbols) and presently calculated (shaded curve) cross section $\sigma_{3,5}$ for double photoionization of Si^{3+} ions using a photon-energy spread $\Delta E = 0.45$ eV. The resonances are associated with the excitation of an $1s$ electron to the $3p$, $4p$, $5p$, and $6p$ subshells. The thick solid line represents the result from a fit of the sum of six Voigt line profiles to the measured data. The resulting fit values are listed in Table 4. Additional fit parameters were ΔE (kept fixed) and a constant background (subtracted from the data). The shaded curve is the present theoretical cross section $\sigma_{3,5}$ shifted in energy by -1.2 eV and convoluted with a Gaussian with an FWHM of 0.45 eV.

Gatuzz et al. (2020) investigated the gaseous component of the ISM using the theoretical absorption data of Witthoeft et al. (2011). In their data, the $1s \rightarrow 3p$ resonance group for neutral silicon is located at $\sim$1839.5 eV in accord with the above considerations. For the other charge states there are significant discrepancies as already noted above. The deviations between the theoretical resonance positions of Witthoeft et al. (2011) and the present experimental ones are 6.7, 4.4, and 9.1 eV for Si^+, Si^{2+}, and Si^{3+}, respectively (Figure 3). All these differences are substantially larger than the uncertainty of the experimental energy scale and they are as large or larger than the energy differences between adjacent charge states (Figure 7(a)). This will lead to a wrong assignment of astronomically observed resonance features if their analysis is based on these theoretical absorption cross sections.

5. Conclusions and Outlook

Using the photon–ion merged-beams technique at a synchrotron light source we have measured cross sections for multiple photoionization of low-charged Si^+, Si^{2+}, and Si^{3+} ions and derived precise absorption data (resonance positions, widths, and strengths) that can be directly used for the astrophysical modeling of the silicon K-shell absorption by interstellar gas clouds and other cosmic objects, as well as for benchmarking the theoretical calculations. From the widths of the core-excited resonances in Si^+ we inferred a value for the core-hole lifetime of $1s$-ionized neutral silicon of 1.4 ± 0.5 fs.

Previously theoretically predicted absorption features deviate significantly in energy from the present experimental findings, whereas the present large-scale MCDHF calculations agree much better with the experimental results. In addition, the

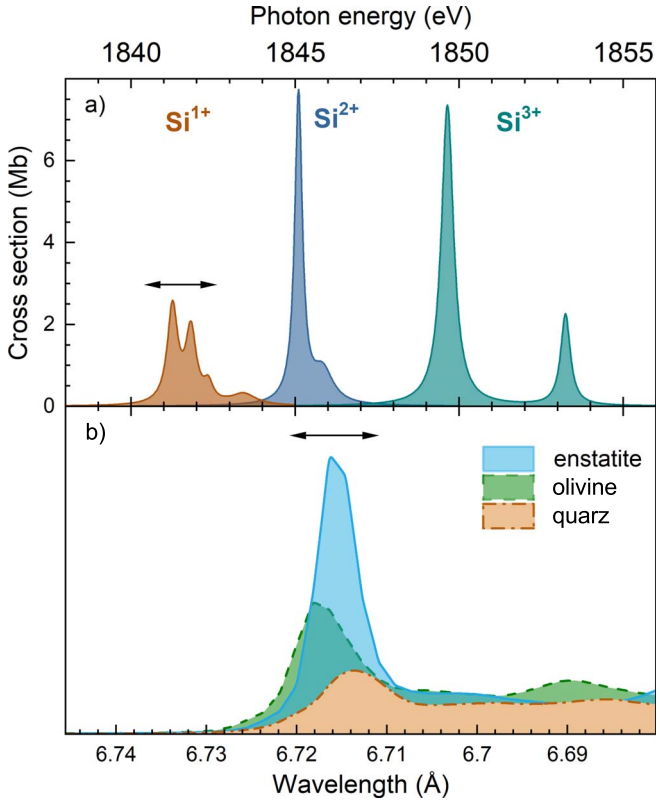

Figure 7. (a) Present results for the Si^{+}, Si^{2+}, and Si^{3+} absorption features that are associated with $1s \rightarrow 3p$ excitations. Each individual resonance is represented as a Lorentzian. The corresponding resonance parameters E_r, Γ, and S_Σ are provided in Tables 2, 3, and 4. (b) Absorption cross sections of some silicon-containing crystalline minerals (Zeegers et al. 2019). The horizontal arrows denote the experimental uncertainties of the photon-energy scales amounting to (a) ±1 eV or ±0.0036 Å and (b) ±1.5 eV or ±0.0055 Å (see the text).

present computations also capture the hole-deexcitation cascades following the initial creation of a K-shell hole. The obtained product charge-state distributions, which are required for an accurate modeling of the charge balance in astrophysical plasmas, agree remarkably well with the experimental results, despite the simplifications that had to be applied to keep the calculations tractable. Current code development aims at systematically expanding such cascade calculations to improve the treatment of the deexcitation processes (Fritzsche 2019; Fritzsche et al. 2021).

When comparing absorption data from different sources the calibration of the photon-energy scales is an issue of concern. The present experimental uncertainty of ±1 eV is sufficient for discriminating between absorption by gaseous and solid silicon-containing matter in the X-ray absorption spectra from the currently operated X-ray telescopes. The accuracy demands will increase with increasing resolving power of future missions such as Athena (Barret et al. 2020). Meeting these demands will require the development of more accurate calibration standards at synchrotron light sources. Promising candidates are few-electron atomic ions that promise calibration uncertainties of less than 10 meV (see, e.g., Müller et al. 2018; Stierhof et al. 2022). Corresponding activities are under way at the PIPE setup.

We acknowledge DESY (Hamburg, Germany), a member of the Helmholtz Association HGF, for the provision of experimental facilities. Parts of this research were carried out at PETRA III and we would like to thank Jens Buck, Moritz Hoesch, Frank Scholz, and Jörn Seltmann for assistance in using beamline P04. This work was supported by the German Federal Ministry for Education and Research (BMBF, grant Nos. 05K16RG1, 05K16GUC, and 05K16SJA) and by the Deutsche Forschungsgemeinschaft (DFG, grant No. 389115454).

ORCID iDs

Stefan Schippers https://orcid.org/0000-0002-6166-7138
Sebastian Stock https://orcid.org/0000-0001-9629-9630
Ticia Buhr https://orcid.org/0000-0003-3337-1740
Alexander Perry-Sassmannshausen https://orcid.org/0000-0002-0700-3875
Michael Martins https://orcid.org/0000-0002-1228-5029
Alfred Müller https://orcid.org/0000-0002-0030-6929
Stephan Fritzsche https://orcid.org/0000-0003-3101-2824

References

Barret, D., Decourchelle, A., Fabian, A., et al. 2020, AN, 341, 224
Beerwerth, R., Buhr, T., Perry-Sassmannshausen, A., et al. 2019, ApJ, 887, 189
Beerwerth, R., & Fritzsche, S. 2017, EPJD, 71, 253
Bizau, J.-M., Mosnier, J.-P., Kennedy, E. T., et al. 2009, PhRvA, 79, 033407
Buth, C., Beerwerth, R., Obaid, R., et al. 2018, JPhB, 51, 055602
Deslattes, R. D., Kessler, E. G., Indelicato, J. P., et al. 2003, RvMP, 75, 35
Fritzsche, S. 2012, CoPhC, 183, 1525
Fritzsche, S. 2019, CoPhC, 240, 1
Fritzsche, S., Palmeri, P., & Schippers, S. 2021, Symmetry, 13, 520
Froese Fischer, C., Tachiev, G., & Irimia, A. 2006, ADNDT, 92, 607
Gatuzz, E., Gorczyca, T. W., Hasoglu, M. F., et al. 2020, MNRAS, 498, L20
Hasoglu, M. F., Gorczyca, T. W., & Manson, S. T. 2021, PhyS, 96, 124024
Henke, B. L., Gullikson, E. M., & Davis, J. C. 1993, ADNDT, 54, 181
Howald, A. M., Gregory, D. C., Meyer, F. W., et al. 1986, PhRvA, 33, 3779
Ibuki, T., Okada, K., Kamimori, K., et al. 2002, SRL, 09, 85
Jenkins, E. B. 2009, ApJ, 700, 1299
Jönsson, P., He, X., Froese-Fischer, C., & Grant, I. P. 2007, CoPhC, 177, 597
Kato, M., Morishita, Y., Oura, M., et al. 2007, in AIP Conf. Proc. 879, Synchrotron Radiation Instrumentation, ed. J.-Y. Choi & S. Rah (Melville, NY: AIP), 1121
Kennedy, E. T., Mosnier, J.-P., Van Kampen, P., et al. 2014, PhRvA, 90, 063409
Kučas, S., Karazija, R., & Momkauskaitė, A. 2012, ApJ, 750, 90
Kučas, S., Momkauskaitė, A., & Karazija, R. 2015, ApJ, 810, 26
Li, D., Bancroft, G. M., Fleet, M. E., & Feng, X. H. 1995, PCM, 22, 115
Mosnier, J.-P., Sayyad, M. H., Kennedy, E. T., et al. 2003, PhRvA, 68, 052712
Müller, A., Bernhardt, D., Borovik, A., Jr., et al. 2017, ApJ, 836, 166
Müller, A., Borovik, A., Jr., Buhr, T., et al. 2015, PhRvL, 114, 013002
Müller, A., Lindroth, E., Bari, S., et al. 2018, PhRvA, 98, 033416
Müller, A., Martins, M., Borovik, A., et al. 2021, PhRvA, 104, 033105
Nagaoka, S., Ibuki, T., Saito, N., et al. 2000, JPhB, 33, L605
Nakanishi, K., & Ohta, T. 2009, JPCM, 21, 104214
Okada, K., Kosugi, M., Fujii, A., et al. 2005, JPhB, 38, 421
Palmeri, P., Quinet, P., Mendoza, C., et al. 2008, ApJS, 177, 408
Perry-Sassmannshausen, A., Buhr, T., Borovik, A., Jr., et al. 2020, PhRvL, 124, 083203
Perry-Sassmannshausen, A., Buhr, T., Martins, M., et al. 2021, PhRvA, 104, 053107
Rogantini, D., Costantini, E., Zeegers, S. T., et al. 2020, A&A, 641, A149
Schippers, S., Beerwerth, R., Abrok, L., et al. 2016a, PhRvA, 94, 041401(R)
Schippers, S., Beerwerth, R., Bari, S., et al. 2021, ApJ, 908, 52
Schippers, S., Buhr, T., Borovik, A., Jr., et al. 2020, XRS, 49, 11
Schippers, S., Kilcoyne, A. L. D., Phaneuf, R. A., & Müller, A. 2016b, ConPh, 57, 215
Schippers, S., Martins, M., Beerwerth, R., et al. 2017, ApJ, 849, 5
Schippers, S., & Müller, A. 2020, Atoms, 8, 45
Schippers, S., Ricz, S., Buhr, T., et al. 2014, JPhB, 47, 115602
Schlachter, A. S., Sant'Anna, M. M., Covington, A. M., et al. 2004, JPhB, 37, L103
Schmelz, H. C., Gaveau, M. A., Reynaud, C., et al. 1995, PhyB, 208-209, 519
Schmidt, E. W., Bernhardt, D., Müller, A., et al. 2007, PhRvA, 76, 032717

Stierhof, J., Kühn, S., Winter, M., et al. 2022, EPJD, 76, 38
Stock, S., Beerwerth, R., & Fritzsche, S. 2017, PhRvA, 95, 053407
Tiesinga, E., Mohr, P. J., Newell, D. B., & Taylor, B. N. 2021, RvMP, 93, 025010
Verner, D. A., Yakovlev, D. G., Band, I. M., & Trzhaskovskaya, M. B. 1993, ADNDT, 55, 233
Viefhaus, J., Scholz, F., Deinert, S., et al. 2013, NIMPA, 710, 151
Witthoeft, M. C., García, J., Kallman, T. R., et al. 2011, ApJS, 1992, 7
Wong, J., Tanaka, T., Rowen, M., et al. 1999, J. Snychr. Rad., 6, 1086
Wuilleumier, F. 1971, J. Physique, 32, C4.88
Zeegers, S. T., Costantini, E., de Vries, C. P., et al. 2017, A&A, 599, A117
Zeegers, S. T., Costantini, E., Rogantini, D., et al. 2019, A&A, 627, A16